Available online at www.sciencedirect.com
ScienceDirect
International Journal of Heat and Fluid Flow 27 (2006) 1028–1042
International Journal of HEAT AND FLUID FLOW
www.elsevier.com/locate/ijhff

Hybrid LES-RANS using synthesized turbulent fluctuations for forcing in the interface region

L. Davidson *, M. Billson

Division of Fluid Dynamics, Department of Applied Mechanics, Chalmers University of Technology, SE-412 96 Göteborg, Sweden

Received 25 January 2005; received in revised form 11 January 2006; accepted 10 February 2006
Available online 17 April 2006

Abstract

The main bottleneck in using Large Eddy Simulations at high Reynolds number is the requirement of very fine meshes near walls. One of the main reasons why hybrid LES-RANS was invented was to eliminate this limitation. In this method unsteady RANS (URANS) is used near walls and LES is used away from walls. The present paper evaluates a method for improving standard LES-RANS. The improvement consists of adding instantaneous turbulent fluctuations (forcing conditions) at the matching plane between the LES and URANS regions in order to trigger the equations to resolve turbulence. The turbulent fluctuations are taken from synthesized homogeneous turbulence assuming a modified von Kármán spectrum. Both isotropic and non-isotropic fluctuations are evaluated. The new approach is applied to fully developed channel flow and it is shown that the imposed fluctuations considerably improve the predictions. It is found that increasing the prescribed turbulent length scale of the synthesized turbulence provides excellent agreement with the classical log-law.

Keywords: LES; Hybrid LES-RANS; DES; Synthesized turbulence; Forcing term; Inlet boundary conditions; Embedded LES

1. Introduction

When simulating bluff body flows, LES (Large Eddy Simulation) is the ideal method. Bluff body flows are dominated by large turbulent scales that can be resolved by LES without too fine a resolution and accurate results can thus be obtained at an affordable cost (Yang and Ferziger, 1993; Rodi et al., 1997; Krajnovic and Davidson, 2005). On the other hand, it is a challenging task to make accurate predictions of wall-bounded flows with LES. The near-wall grid spacing should be about one wall unit in the wall-normal direction. This is similar to the requirement in RANS (Reynolds-Averaged Navier–Stokes) using low-*Re* number models. The resolution requirements in wall-parallel planes for a well-resolved LES in the near-wall region expressed in wall units are approximately 100 (streamwise) and 30 (spanwise). This enables resolution of the near-wall turbulent structures in the viscous sub-layer and the buffer layer consisting of high-speed in-rushes and low-speed ejections (Robinson, 1991), often called the streak process. At low to medium Reynolds numbers the streak process is responsible for the major part of the turbulence production. These structures must be resolved in an LES in order to achieve accurate results. Thus, for wall-bounded flows at high Reynolds numbers of engineering interest, the computational resource requirement of accurate LES is prohibitively large. Indeed, the requirement of near-wall grid resolution is the main reason why LES is too expensive for engineering flows, which was one of the lessons learned in the LESFOIL project (Davidson et al., 2003; Mellen et al., 2003).

The object of hybrid LES-RANS (Xiao et al., 2003; Davidson and Peng, 2003; Temmerman et al., 2002; Tucker and Davidson, 2004; Tucker, 2003) is to eliminate the requirement of high near-wall resolution in wall-parallel planes. In the near-wall region (the URANS region), a

* Corresponding author. Fax: +46 31 18 09 76.
E-mail address: lada@chalmers.se (L. Davidson).
URL: http://www.tfd.chalmers.se/~lada (L. Davidson).

0142-727X/$ - see front matter © 2006 Elsevier Inc. All rights reserved.
doi:10.1016/j.ijheatfluidflow.2006.02.025

low-*Re* number RANS turbulence model (usually an eddy-viscosity model) is used. In the outer region (the LES region), the usual LES is used, see Fig. 1. The idea is that the effect of the near-wall turbulent structures should be modelled by the RANS turbulence model rather than being resolved. In the LES region, coarser grid spacing in wall-parallel planes can be used. The grid resolution in this region is presumably dictated by the requirement of resolving the largest turbulent scales in the flow (which are related to the outer length scales, e.g. the boundary layer thickness) rather than the near-wall turbulent processes. The unsteady momentum equations are solved throughout the computational domain. The turbulent RANS viscosity is used in the URANS region, and the turbulent SGS viscosity is used in the LES region.

Much work on hybrid LES-RANS has recently been carried out (Xiao et al., 2003; Davidson and Peng, 2003; Temmerman et al., 2002; Tucker and Davidson, 2004; Tucker, 2003; Hamba, 2003; Temmerman et al., 2005; Dejoan and Schiestel, 2001; Kenjereš and Hanjalić, 2005). In Xiao et al. (2003), Davidson and Peng (2003), Hamba (2003) two-equation models were used in the URANS region and a one-equation SGS model was employed in the LES region. One-equation models were used in both regions in Tucker and Davidson (2004), Tucker (2003). The locations of the matching planes were determined in different ways. In some work (Davidson and Peng, 2003; Hamba, 2003) it was chosen along a pre-selected grid plane. In Tucker and Davidson (2004) it was determined by comparing the URANS and the LES turbulent length scales or was computed from turbulence/physics requirements. Xiao et al. (2003) used a two-equation model in the URANS region and blended it into a one-equation model in the LES region. Different partial differential equations for automatically finding the matching plane were investigated in Tucker (2003). A one-equation model was used in both regions in Temmerman et al. (2005), and the c_μ coefficient at the interface was computed dynamically to yield a smoother transition between the URANS and LES regions. Dejoan and Schiestel (2001) proposed a k–ε turbulence model, later also used by Kenjereš and Hanjalić (2005), in which the $c_{\varepsilon 2}$ is made into a function of the ratio of the RANS and LES length scales. On a fine mesh the model switches smoothly to LES and in the limit $c_{\varepsilon 1} = c_{\varepsilon 2}$ so that a pure DNS solution is obtained.

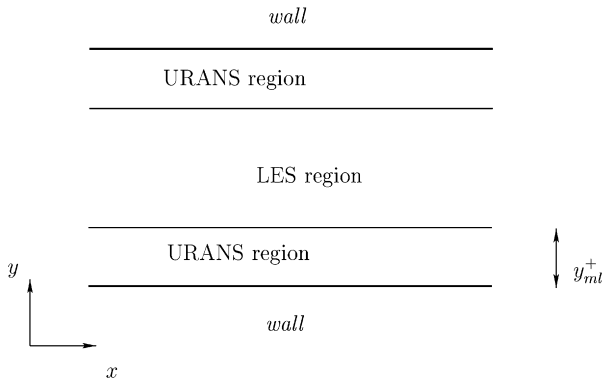

Fig. 1. The LES and URANS region.

Hybrid LES-RANS is similar to DES (detached eddy simulations) (Spalart et al., 1997; Spalart, 2000; Strelets, 2001). The main difference is that the original DES aims at covering the whole attached boundary layer with URANS, whereas in the present work hybrid LES-RANS aims at covering only the inner part of the boundary layer with URANS. In later work DES has been used as a wall model (Nikitin et al., 2000; Piomelli et al., 2003), and, in this form, DES is similar to the present hybrid LES-RANS without forcing.

Although good results have been presented using hybrid LES-RANS, it has been found that the treatment of the interface between the URANS region and the LES region is crucial for the success of the method. The resolved turbulence supplied by the URANS region to the LES region has no reasonable turbulent characteristics and is not appropriate for triggering the LES equations to resolve turbulence. This results in too poorly resolved stresses in the interface region and thereby gives a ramp – also referred to as a shift – in the velocity profile approximately at the location of the matching plane (Davidson and Peng, 2003; Nikitin et al., 2000; Davidson and Dahlström, 2005b; Hamba, 2003; Temmerman et al., 2002; Tucker and Davidson, 2004; Piomelli et al., 2003). The overly small resolved stresses in the LES region are translated into too small a wall shear stress. Several modifications have been proposed to remove this deficiency. Temmerman et al. (2002, 2005) suggested dampening the modelled stresses in the URANS region to reduce the total (i.e. resolved plus modelled) shear stress in the URANS region and thereby reduce the jump in shear stress across the matching plane. Numerical smoothing was used at the interface in Tucker and Davidson (2004). Hamba (2003) proposed a modification of the discretized streamwise equation at the interface in order to avoid filtering out any resolved fluctuations at the interface. In Piomelli et al. (2003) backscatter was introduced in the interface region with the object of generating resolved fluctuations.

In the present paper we propose adding fluctuations to the momentum equations at the interface. The turbulent fluctuations are taken from synthesized homogeneous turbulence assuming a modified von Kármán spectrum. Both isotropic and non-isotropic fluctuations are evaluated. No streamwise momentum is injected in the former case (since there is no correlation between the added fluctuations in the streamwise and wall-normal direction), whereas in the latter case the added fluctuations yield a source term in the streamwise momentum equation. The object is to trigger the equations to resolve turbulence. How large a part of the turbulent spectrum that is resolved depends entirely on the resolution. The momentum equations are solved in the entire domain and the turbulent viscosity is in both regions obtained from a one-equations k_{sgs} equation and an algebraic length scale.

For comparison, fluctuations are also taken from a separate DNS simulation, an approach recently described in Davidson and Dahlström (2005b). An interesting, and rather similar, approach was presented by Batten et al. (2004), in which synthetic turbulent fluctuations was used to trigger the resolved turbulence when going from an URANS region to an LES region. In a study by Larsson et al. (2005), an approach fairly similar to the present method was presented. Hybrid LES-RANS was used and synthetic fluctuations were employed as forcing in the URANS region.

Adding fluctuations in order to trigger the equations to resolve turbulence is actually very similar to prescribing fluctuating turbulent inlet boundary conditions for DNS or LES (or hybrid LES-RANS). If no triggering inlet boundary conditions are prescribed in DNS or LES, the resolved turbulence near the inlet will be too small and a large streamwise distance is required before the equations trigger themselves into describing turbulent flow. This is also the case in hybrid LES-RANS: if no triggering (forcing) is applied at the interface between the LES region and the URANS region, the resolved turbulence in the LES region near the URANS region will be too small.

The paper is organized as follows. The method for generating synthetic fluctuations is first presented, after which the equations and the numerical method are given. In the section that follows we present the DNS simulation from which the DNS fluctuations are generated. The hybrid LES-RANS method and the approach used to introduce forcing fluctuations are then described. The results are reported and discussed, the issue of overly large total turbulent kinetic energy is addressed, and, finally, conclusions are drawn.

2. Synthesized turbulence

2.1. Isotropic fluctuations

A turbulent velocity field can be simulated using random Fourier modes. This was proposed by Kraichnan (1970) and further developed by Karweit et al. (1991), Lee et al. (1992), Bechara et al. (1994), Bailly and Juvé (1999). The velocity field is given by

$$u_i'(x_j) = 2\sum_{n=1}^{N} \hat{u}^n \cos\left(\kappa_j^n x_j + \psi^n\right)\sigma_i^n \tag{1}$$

where $\hat{u}^n$, ψ^n and σ_i^n are amplitude, phase and direction of Fourier mode n. The synthesized turbulence is generated as follows. The notation follows that in Billson (2004), Billson et al. (2003) and more information is given in these papers.

(1) For each mode n, create random angles φ^n, α^n and θ^n (see Figs. 2 and 3) and random phase ψ^n. The probability distributions are given in Table 1.
(2) Define the highest wave number based on mesh resolution $\kappa_{\max} = 2\pi/(2\Delta)$, where Δ is the smallest grid spacing at the x–z interface plane.

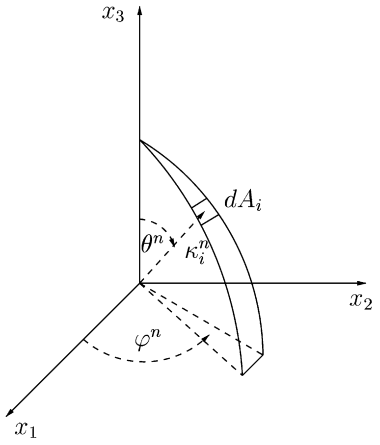

Fig. 2. The probability of a randomly selected direction of a wave in wave-space is the same for all dA_i on the shell of a sphere.

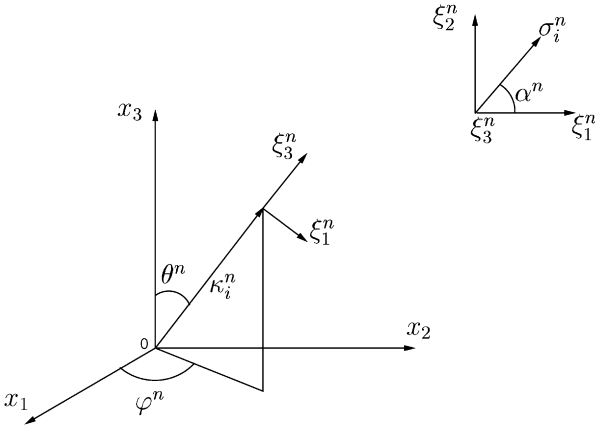

Fig. 3. The wave number vector, κ_i^n, and the velocity unit vector, σ_i^n, are orthogonal (in physical space) for each wave number n. The unit vector, σ_i^n, is defined such that $\sigma_i^n \kappa_i^n = 0$ (superscript n denotes Fourier mode n). Furthermore, σ_3^n is parallel to κ_i^n (i.e. $\sigma_3^n = \xi_3^n$). The direction of σ_i^n in the ξ_1^n–ξ_2^n plane is randomly chosen through α^n.

Table 1
Probability distributions of the random variables

$p(\varphi^n) = 1/(2\pi)$	$0 \leqslant \varphi^n \leqslant 2\pi$
$p(\psi^n) = 1/(2\pi)$	$0 \leqslant \psi^n \leqslant 2\pi$
$p(\theta^n) = 1/2\sin(\theta)$	$0 \leqslant \theta^n \leqslant \pi$
$p(\alpha^n) = 1/(2\pi)$	$0 \leqslant \alpha^n \leqslant 2\pi$

(3) Define the smallest wave number from $\kappa_1 = \kappa_e/p$ where $\kappa_e = \alpha 9\pi/(55L_t)$, $\alpha = 1.453$, see Fig. 4. Factor p should be larger than one to make the largest scales larger than those corresponding to κ_e, and in the present work $p = 2$.
(4) Divide the wave number space $\kappa_{\max} - \kappa_1$ into $N = 150$ modes, equally large, of size $\Delta\kappa$.
(5) Compute the randomized components of κ_j^n according to Fig. 2.
(6) Continuity requires that the unit vector, σ_i^n, and κ_j^n are orthogonal. σ_3^n is arbitrarily chosen to be parallel to κ_i^n (see Fig. 3), and α^n and the requirement of orthogonality give the remaining two components.

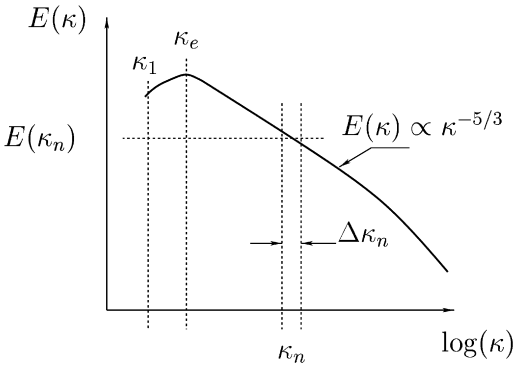

Fig. 4. Modified von Kármán spectrum.

(7) A modified von Kármán spectrum is chosen, see Eq. (2) and Fig. 4. The amplitude $\hat{u}^n$ of each mode in Eq. (1) is then obtained from $\hat{u}^n = (E(|\kappa_j^n|)\Delta\kappa)^{1/2}$.
(8) Having $\hat{u}^n$, κ_j^n, σ_i^n and ψ^n, allows computation of the expression in Eq. (1).

$$E(\kappa) = \alpha \frac{u_{\text{rms}}^2}{\kappa_e} \frac{(\kappa/\kappa_e)^4}{[1+(\kappa/\kappa_e)^2]^{17/6}} e^{[-2(\kappa/\kappa_\eta)^2]}$$
$$\kappa = (\kappa_i \kappa_i)^{1/2}, \quad \kappa_\eta = \varepsilon^{1/4} \nu^{-3/4} \tag{2}$$

2.2. Non-isotropic fluctuations

An approach for using the method described above for synthesizing non-isotropic turbulent fluctuations has recently been proposed (Smirnov et al., 2001; Billson et al., 2004; Billson, 2004). The approach can be summarized as follows (Billson et al.):

(1) The Reynolds stress tensor and a turbulent length scale are supplied (in the present work, they are taken from DNS at the location of the matching plane).
(2) The principal coordinate directions of the Reynolds stress tensor are computed and the eigenvalues, i.e. the normal Reynolds stresses in the principal coordinate system, are computed.
(3) The method described in the previous section is used to generate isotropic turbulent fluctuations, $u_{i,S}^{\star\prime}$, in the principal coordinate system (denoted by superscript ★). The generated isotropic fluctuations are re-scaled so that $\langle (u_{i,S}^{\star\prime})^2 \rangle = \langle (u_{i,\text{DNS}}^{\star\prime})^2 \rangle$. Note that, although $\langle (u_{i,S}^{\star\prime})^2 \rangle \neq \langle (u_{j,S}^{\star\prime})^2 \rangle$ $(i \neq j)$, the shear stresses in the principal coordinate system are zero.
(4) In order to satisfy continuity the length scales of the synthesized non-isotropic fluctuations are re-scaled making the turbulent length scales larger in the principal direction of the largest fluctuations and vice versa.
(5) The synthesized fluctuations are transformed back to the original coordinate system. In this coordinate system the Reynolds stresses of the synthesized fluctuations are equal to the supplied DNS Reynolds stress tensor (see item 1 above). This means in particular that the shear stresses are non-zero (provided that the same was the case for the supplied DNS Reynolds stress tensor).

3. Equations and numerical method

3.1. Momentum and continuity equations

The incompressible Navier–Stokes equations with an added turbulent/SGS viscosity read

$$\frac{\partial \bar{u}_i}{\partial t} + \frac{\partial}{\partial x_j}(\bar{u}_i \bar{u}_j) = \delta_{1i} - \frac{1}{\rho}\frac{\partial \bar{p}}{\partial x_i} + \frac{\partial}{\partial x_j}\left[(\nu + \nu_{\text{T}})\frac{\partial \bar{u}_i}{\partial x_j}\right] \tag{3}$$

$$\frac{\partial \bar{u}_i}{\partial x_i} = 0 \tag{4}$$

where $\nu_{\text{T}} = \nu_{\text{t}}$ (ν_{t} denotes the turbulent RANS viscosity) for $y \leqslant y_{ml}$ (see Fig. 1) and, for $y > y_{ml}$, $\nu_{\text{T}} = \nu_{\text{sgs}}$. The turbulent viscosity, ν_{T}, is computed from an algebraic turbulent length scale (see Table 2) and k_{T}; the latter is obtained by solving its transport equation, see Eq. (8). The first term on the right-hand side is the constant driving pressure gradient. The Reynolds number is defined as $Re_\tau = u_\tau \delta/\nu$, where δ denotes channel half width and u_τ denotes friction velocity related to the driving pressure gradient. The $\partial\bar{p}/\partial x_i$ corresponds to the fluctuating pressure gradient term whose mean is zero. All quantities in Eqs. (3) and (4) have been scaled with u_τ and δ, and $\rho = u_\tau = \delta = 1$ and $\nu = 1/Re_\tau$.

No-slip conditions are used at the walls and periodic boundary conditions are used in the streamwise direction (x) and the spanwise direction (z). Neumann boundary conditions are used for pressure at the walls.

3.2. Numerical method

The numerical solver is based on the fractional step method (Chorin, 1968). Second-order central differencing in space is used for all terms. An implicit, two-step time-advancement method is employed for the pressure–velocity coupling. The discrete form of Eq. (3) can be written as

$$\bar{u}_i^{n+1/2} = \bar{u}_i^n + \Delta t H\left(\bar{u}_i^n, \bar{u}_i^{n+1/2}\right) - \frac{1}{\rho}\alpha\Delta t \frac{\partial \bar{p}^{n+1/2}}{\partial x_i} - \frac{1}{\rho}(1-\alpha)\Delta t \frac{\partial \bar{p}^n}{\partial x_i} \tag{5}$$

Table 2
Turbulent viscosities and turbulent length scales in the URANS and LES regions

	URANS region	LES region
ℓ	$2.5n[1-\exp(-0.2k^{1/2}n/\nu)]$	$\ell = \Delta = (\delta V)^{1/3}$
ν_{T}	$2.5k^{1/2}n[1-\exp(-0.014k^{1/2}n/\nu)]$	$0.07k_{\text{sgs}}^{1/2}\ell$
C_ε	1.0	1.07

n denotes the distance to the nearest wall.

where $H(\bar{u}_i^n, \bar{u}_i^{n+1/2})$ includes the driving pressure gradient, the convection term, and the viscous and the turbulent stresses, and $\alpha = 0.5$ (the Crank–Nicholson scheme). Eq. (5) gives $\bar{u}_i^{n+1/2}$, which does not satisfy continuity. An intermediate velocity field is computed by subtracting the implicit part of the pressure gradient, i.e.

$$\bar{u}_i^* = \bar{u}_i^{n+1/2} + \frac{1}{\rho}\alpha\Delta t \frac{\partial \bar{p}^{n+1/2}}{\partial x_i} \tag{6}$$

Now $\bar{u}_i^{n+1/2}$ and $\bar{p}_i^{n+1/2}$ in Eq. (6) are replaced by the velocity and pressure field at level $(n+1)$, i.e. $\bar{u}_i^{n+1}$ and $\bar{p}_i^{n+1}$. Taking the divergence of Eq. (6) and setting the requirement that the face velocities, $\bar{u}_{i,f}^{n+1}$ (which are obtained by linear interpolation), satisfy the continuity equation, the following Poisson equation for pressure is obtained

$$\frac{\partial^2 \bar{p}^{n+1}}{\partial x_i \partial x_i} = \frac{\rho}{\Delta t \alpha}\frac{\partial \bar{u}_{i,f}^*}{\partial x_i} \tag{7}$$

The Poisson equation is solved with an efficient multigrid method (Emvin, 1997). The sequence of solving Eqs. (5)–(7) is repeated each time step until the momentum and continuity equations are satisfied. For greater detail, see Davidson and Peng (2003).

4. Direct numerical simulations

In the present paper the fluctuations for the forcing described above are obtained from synthesized turbulence. For comparison the fluctuations are also taken from a DNS as in Davidson and Dahlström (2005b). To generate the fluctuations a DNS was made of channel flow at $Re_\tau = 500$. The finite volume method presented above was used. The extent of the computational domain was $2\pi \times 2 \times 0.5\pi$ (x, y, z). Two DNS simulations were carried out, one with $64 \times 64 \times 64$ cells and one with $96 \times 96 \times 96$ cells. The first near-wall computational node was located at $y^+ = 0.3$ for both meshes and the geometric stretching in the y-direction was 17% for the 64^3 mesh and 8% for the 96^3 mesh.

The streamwise velocity profile and the resolved RMS fluctuations are compared in Fig. 5 with the DNS in Moser et al. (1999) at $Re_\tau = 595$. As can be seen, the agreement is good.

Using inner scaling (u_τ and ν) the turbulence structure in the inner logarithmic region is only weakly dependent on Reynolds number. It is thus believed that these data can be used for forcing at the interface for a wide range of boundary layers and that they possess realistic structural information. One aspect of this is shown in Fig. 6a, which shows scatter plots for quadrant analysis of the u' and v' fluctuations at $y^+ = 60$. As expected, quadrant 2 (negative u' and positive v') and quadrant 4 (positive u' and negative v') dominate. This is also the case for the synthesized non-isotropic fluctuations, see Fig. 6b. The events corresponding to these two quadrants contribute to a negative $\langle u'v' \rangle$ correlation.

5. Hybrid LES-RANS

5.1. The equation for turbulent kinetic energy

A one-equation model is employed in both the URANS region and the LES region, which reads

$$\frac{\partial k_T}{\partial t} + \frac{\partial}{\partial x_j}(\bar{u}_j k_T) = \frac{\partial}{\partial x_j}\left[(\nu + \nu_T)\frac{\partial k_T}{\partial x_j}\right] + P_{k_T} - C_\varepsilon \frac{k_T^{3/2}}{\ell} \tag{8}$$
$$P_{k_T} = -\tau_{ij}\bar{s}_{ij}, \quad \tau_{ij} = -2\nu_T \bar{s}_{ij}$$

In the inner region ($y \leqslant y_{ml}$) k_T corresponds to the RANS turbulent kinetic energy, k; in the outer region ($y > y_{ml}$) it corresponds to the subgrid-scale kinetic turbulent energy (k_{sgs}). No special treatment is used in the equations at the matching plane except that the form of the turbulent viscosity and the turbulent length scale are different in the two regions, see Table 2. At the walls, $k_T = 0$.

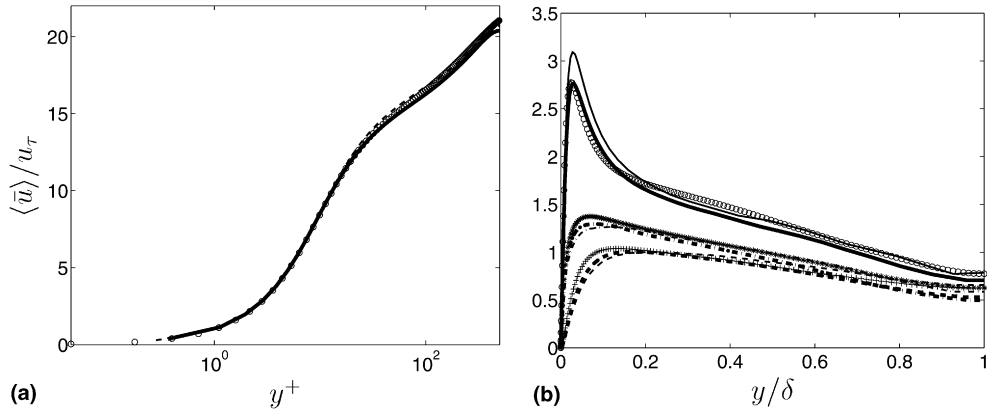

Fig. 5. Streamwise $\langle \bar{u} \rangle$ profiles and resolved RMS fluctuations. Thick lines: present 96^3 DNS; thin lines: present 64^3 DNS; markers: DNS Moser et al. (1999). (a) Velocity profile and (b) RMS fluctuations.

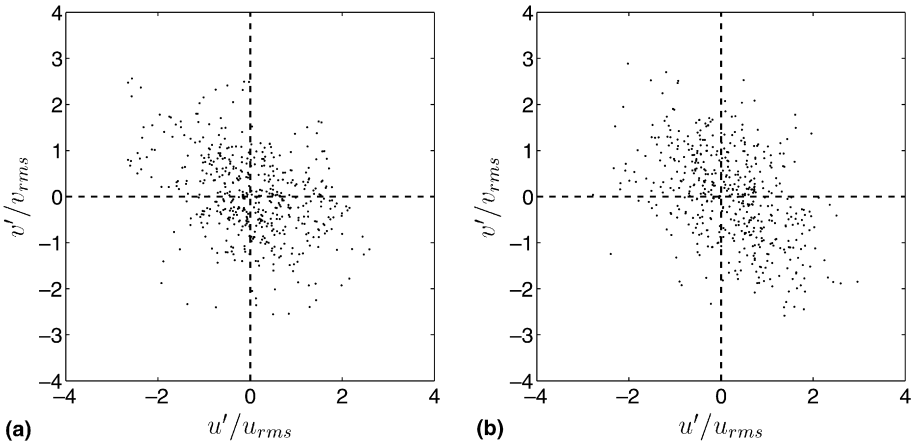

Fig. 6. Scatter plot of u' and v' fluctuations at $y^+ = 60$. (a) Present 96^3 DNS. (b) Synthesized non-isotropic turbulence.

5.2. Forcing conditions

This section describes how forcing conditions are implemented and how the synthesized fluctuations and DNS fluctuations are mapped to the CFD domain.

Using standard LES-RANS for a fully developed channel flow, the ratio of the centerline velocity to the friction velocity, U_c/u_τ, is too large, which indicates that the turbulent diffusion is too small. To increase the turbulent resolved diffusion, forcing fluctuations are added to trigger the equations to resolve large-scale turbulence. If the mesh is very coarse, as is usually the case in hybrid LES-RANS, the turbulence that the momentum equations describe will not correspond to real turbulence, but this will at least increase the resolved turbulent diffusion in the wall-normal direction, which is the chief objective. Ratio U_c/u_τ will thus be decreased by the increased turbulence diffusion generated by the forcing term. If the mean of this forcing term is non-zero, it should, in order to increase the wall shear stress, be positive. Since the forcing term will be added in a finite volume context, we integrate the term in the streamwise momentum equation over the control volume and obtain

$$-\int_V \frac{\partial u'_f v'_f}{\partial y}\,\mathrm{d}V = F_{j+1/2}A_n - F_{j-1/2}A_n = -(u'_f v'_f)_{j+1/2} - 0 = -u'_f v'_f A_n = -\frac{u'_f v'_f \Delta V}{\Delta y} \tag{9}$$

$F_{j+1/2} = -u'_f v'_f$ and $F_{j-1/2} = 0$ denote the forcing fluxes at face $j + 1/2$ and $j - 1/2$, respectively. ΔV, A_n and Δy denote the volume, the face area and the length of the wall-normal cell side of the control volume, respectively, see Fig. 7. u'_f and v'_f (index f is either DNS or S) denote the forcing fluctuating velocity components in the x and y directions, respectively. When the forcing fluctuations are taken from a DNS or from synthesized non-isotropic fluctuations, the correlation between u'_f and v'_f will be negative and hence the right-hand side of Eq. (9) will be positive, as required. More important, the added fluctuations also give rise to an additional production term in the equation for resolved, turbulent kinetic energy, see Eq. (20) and Table 3.

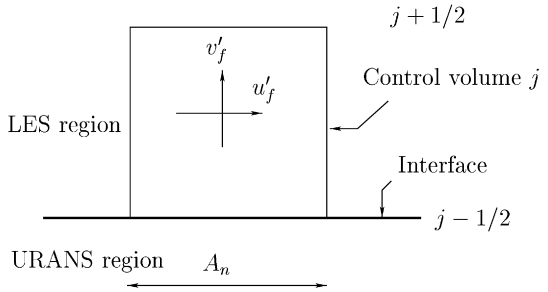

Fig. 7. Added fluctuations, u'_f, v'_f, w'_f, in a control volume ($j = j_{ml} + 1$) in the LES region adjacent to the interface. The fluctuations are either synthesized (subscript $f = S$) or taken from channel DNS (subscript $f =$ DNS).

The right-hand side of Eq. (9) can be regarded as a flux term by which u'_f fluctuations are advected by v'_f. Hence the sources for the three momentum equations are taken as

$$S_U = -\gamma\rho u'_f v'_f A_n, \quad S_V = -\gamma\rho v'_f v'_f A_n, \quad S_W = -\gamma\rho w'_f v'_f A_n \tag{10}$$

Table 3
Presentation of test cases

Forcing	M_{DNS}	M_S	$u_{*,w}$	$P_{k,f}$
None	–	–	1	–
DNS	0.5	–	1.15	160
DNS	0.25	–	1.15	170
Isotropic	–	1	1	150
Isotropic	–	0.25	1	190
Non-isotropic	–	1	1.18	160
Non-isotropic	–	0.25	1.18	230
White noise ($\gamma \equiv 1.4$)	0.25	–	1	420

Type of forcing used; values of M_S and M_{DNS} used for mapping (see Eqs. (14) and (15)); the predicted friction velocity ($\tau_w = u^2_{*,w}$); the additional production, $P_{k,f}$ (see Eq. (20)), due to the added fluctuations.

where

$$\gamma = c_\gamma k_T(x, y_{ml}, z)/k_f, \quad k_f = \frac{1}{2}\left(u^2_{f,\mathrm{rms}} + v^2_{f,\mathrm{rms}} + w^2_{f,\mathrm{rms}}\right) \tag{11}$$

For DNS fluctuations the c_γ coefficient was in Davidson and Dahlström (2005b) optimized to $c_\gamma = 0.4$ and this value was used in all simulations in the present work. It should be noted that using a value of $c_\gamma = 1$ in connection with isotropic synthetic fluctuations has a negligible influence on the results compared to $c_\gamma = 0.4$. A change in c_γ changes the amplitude of the forcing fluctuations, but for isotropic fluctuations it does not affect the injected momentum parallel to the wall (it is zero).

In fully developed channel flow with streamwise periodic boundary conditions, as in the present work, global momentum balance requires that the driving pressure gradient is equal to the sum of the two wall shear stresses. When a forcing term is added to the streamwise momentum equation, the global momentum balance is modified and reads (Eq. (3) integrated from $(0,0,0)$ to $(x_{\max}, 2\delta, z_{\max})$ and in time)

$$\begin{aligned} &2\delta x_{\max} z_{\max} - 2\gamma\langle u'_f v'_f\rangle x_{\max} z_{\max} = 2\tau_w x_{\max} z_{\max} \\ &\quad \Rightarrow\ \tau_w = 1 - \langle \gamma u'_f v'_f\rangle \end{aligned} \tag{12}$$

For DNS and non-isotropic fluctuations, $-\langle u'_f v'_f\rangle > 0$ and hence $\tau_w = \rho u^2_{*,w} > 1$ (see Table 3). For isotropic fluctuations, $-\langle u'_f v'_f\rangle = 0$ and hence the source $S_U = 0$.

5.3. Mapping of forcing fluctuations to the CFD domain

Synthesized turbulence is generated as a single realization in a large two-dimensional ξ–ζ plane that extends $z_{\max}$ (32 cells of size Δz) in the z-direction and $5000\Delta x$ (50 000 cells of size $0.1\Delta x$) in the x-direction. To map the synthesized turbulence at each time step to the computational domain, it is assumed that the ξ–ζ plane is convected at a constant speed, V_S, in the x-direction, see Fig. 8. V_S is taken as the time-averaged velocity at the location of the matching plane, i.e. $V_S = \langle \bar{u}\rangle_{y_{ml}}$. In this way the u'_S fluctuation, for example, is mapped from the ξ–ζ plane to the x–z CFD plane as

$$u'_S(x, y_{ml}, z, t) = u'_S(\xi, z), \quad \xi = V_S t + x_{\max} - x \tag{13}$$

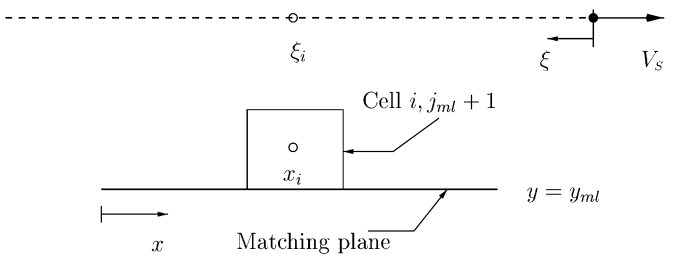

Fig. 8. Mapping of synthesized fluctuations from the ξ–ζ plane (dashed line) to the computational x–z plane at $y = y_{ml}$, see Eq. (14). $\Delta x = 10\Delta\xi$. The ξ–ζ plane is moving to the right at speed $V_S = \langle \bar{u}_{j_{ml}+1}\rangle$.

The mapping is similar to Taylor's hypothesis. In discrete form for cell I it reads

$$\xi_I = 10 M_S (V_S t + x_{\max} - x_I)/\Delta x \tag{14}$$

(factor 10 appears because $\Delta x/\Delta\xi = 10$). Different values of M_S have been used, see Table 3. A low M_S value gives an increased streamwise turbulent length scale. Note that it is important that V_S is constant (i.e. time independent) in Eq. (14), so that the length scales in the ξ–ζ domain are properly translated to length and time scales in the CFD domain; constant V_S was found to be less important in Eq. (15).

The DNS fluctuations are generated as a time series at $x = 0$ along the z-direction from the present 64^3 simulations. The Taylor hypothesis is used to map DNS fluctuations from the time domain (τ) to the matching plane at each instant (Davidson and Dahlström, 2005b). For the streamwise fluctuation, for example, we get

$$\begin{aligned} &u'_{\mathrm{DNS}}(x, y_{ml}, z, t) = u'_{\mathrm{DNS}}(x = 0, y_{ml}, z, \tau), \\ &\tau = M_{\mathrm{DNS}}(t - x/V_S) \\ &V_S = \langle \bar{u}_{y_{ml}}\rangle. \end{aligned} \tag{15}$$

For greater detail, see Davidson and Dahlström (2005b).

6. Results

6.1. The mesh

A coarse mesh was purposely chosen. The mesh has 32 cells in both the streamwise (x) and the spanwise (z) direction. The size of the computational domain is $x_{\max} = 4\pi$, $y_{\max} = 2$ (geometric stretching of 17%) and $z_{\max} = 2\pi$. This gives a Δx^+ and Δz^+ of approximately 785 and 393, respectively. In outer scaling, it gives $\Delta x/\delta = 0.4$ and $\Delta z/\delta = 0.2$. The location of the matching plane is at $y = 0.031$ (lower wall), which corresponds to $y^+ = 62$ and 11 cells ($=j_{ml} - 1$) in the URANS region at each wall. Care has been taken to ensure that all results presented are independent of the size of the computational domain. It should be mentioned that on this mesh a pure LES is not able to sustain any resolved turbulence at all, but a steady solution is obtained.

6.2. The influence of forcing conditions

Fully developed channel flow at $Re_\tau = u_\tau\delta/\nu = 2000$ (δ denotes the channel half width) is used as a test case to evaluate the effect of different forcing conditions. This flow may seem to be an easy test case, but it is not. In attempts to improve the performance of LES in wall-bounded flows, the Achilles' heel is the near-wall flow region. The bulk velocity in fully developed channel flow with periodic boundary conditions (see Eq. (3)) is entirely determined by the wall shear stress; consequently the flow is extremely sensitive to the turbulence in the near-wall region.

The streamwise velocity profiles obtained with and without forcing are compared in Fig. 9 with the present DNS

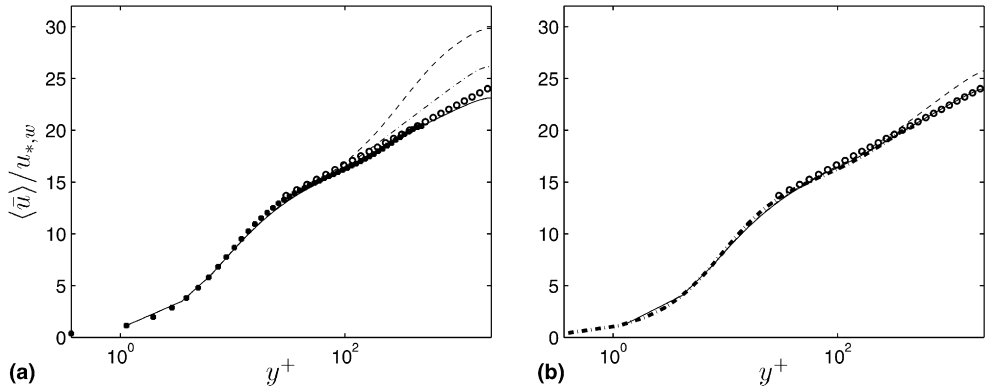

Fig. 9. Streamwise velocities. $\langle \bar{u} \rangle$ profiles. ○: $2.5\ln(y^+) + 5.2$. (a) Solid lines: isotropic forcing, $M_S = 0.25$; dash-dotted lines: isotropic forcing, $M_S = 1$; dashed lines: no forcing; +: present 96^3 DNS. (b) DNS forcing. Solid line: $M_{\mathrm{DNS}} = 0.25$; dashed line: $M_{\mathrm{DNS}} = 0.5$.

and the log-law. It can be seen that the centerline velocity is strongly over-predicted when no forcing is used, whereas forcing with $M_S = M_{\mathrm{DNS}} = 0.25$ gives excellent agreement with the log-law. The reason for the overly large velocities without forcing is that the resolved shear is too small. It can be seen in Fig. 10a that it is the resolved shear stress that increases when forcing is introduced, indicating that the resolved shear stress without forcing is too small. This was also observed by Piomelli et al. (2003): when forcing is introduced, the resolved shear stress increases, which reduces the bulk and centerline velocity.

The main argument for introducing forcing conditions is that the LES region adjacent to the interface plane is supplied with poor boundary conditions from the URANS region. Although the flow coming from the URANS region is indeed unsteady (it is triggered by the LES region) it does not have any properly resolved turbulent structures. The length scales and time scales of the unsteadiness in the URANS region are not able to trigger the equations in the LES region into resolving turbulence. An example of this can be seen in Fig. 11 where two-point correlations of $u'u'$ are shown for hybrid LES-RANS with and without forcing conditions and are compared with 96^3 DNS data. Here we find that the streamwise two-point correlation for hybrid LES-RANS without forcing conditions is very large indeed. This is a good illustration of the lack of proper turbulent structures in the URANS region (the two-point correlation is almost constant in the entire URANS region [not shown]). When forcing conditions are added the streamwise two-point correlation is drastically reduced, although it does not reach the low values of the DNS data. In Fig. 11a it can be seen that the magnitude of the DNS streamwise integral length scale is roughly equal to the grid spacing in the hybrid LES-RANS simulations. Thus it is not reasonable to expect that the hybrid LES-RANS would yield such a small streamwise two-point correlation as the DNS.

Whereas the streamwise two-point correlation is strongly affected when forcing is used, the two-point correlation in the z-direction is hardly affected at all, see Fig. 11b. The reason is that the spanwise correlation without forcing is reasonable well predicted on the given grid and cannot be further reduced (if it were the spanwise correlation would be zero for $\zeta > \Delta z$).

The added fluctuations (DNS or synthesized) include both large and small scales. It could be argued that only the small turbulent scales, which are modelled in the URANS region, need to be added to the momentum

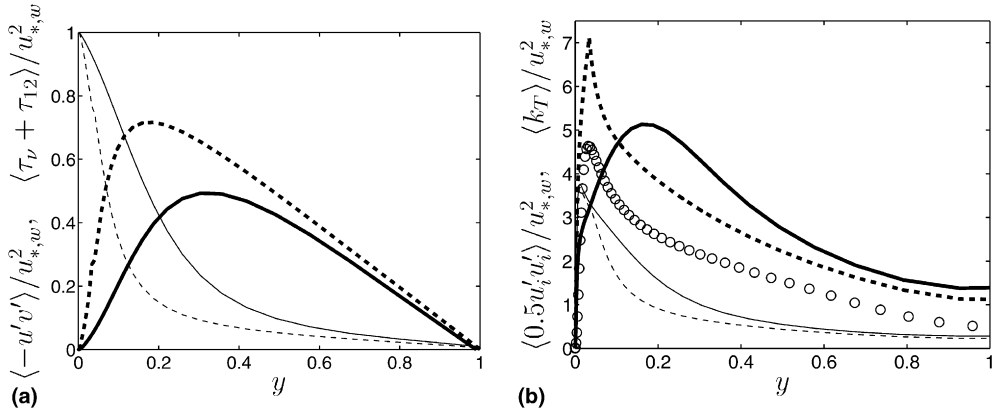

Fig. 10. Shear stress and turbulent kinetic energy. Solid lines: no forcing; dashed lines: forcing with isotropic fluctuations with $M_S = 0.25$; ○: present 96^3 DNS. Thick lines: resolved; thin lines: modelled. (a) Shear stresses. τ_ν denotes viscous stress. (b) Turbulent kinetic energy.

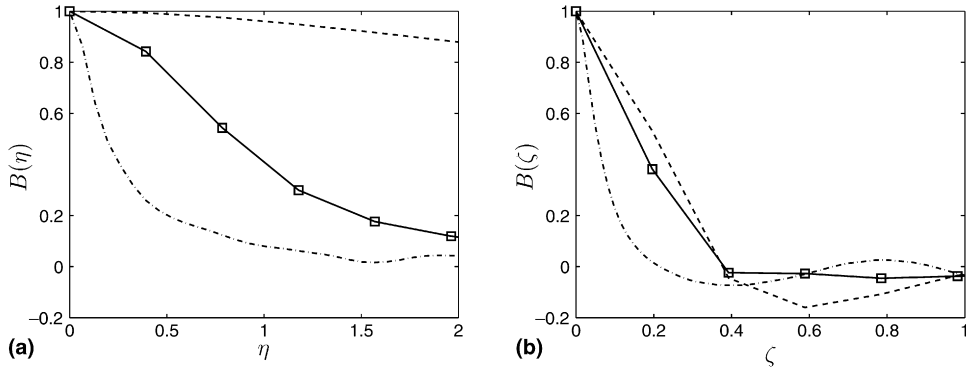

Fig. 11. Two-point correlations at $y = y_{ml}$. Solid lines: forcing with isotropic fluctuations with $M_S = 0.25$; dashed lines: no forcing; dash-dotted lines: present 96^3 DNS. Markers indicate the grid resolution. (a) $B(\eta) = \langle u'(x)u'(x+\eta)\rangle/u^2_{\rm rms}$. (b) $B(\zeta) = \langle u'(z)u'(z+\zeta)\rangle/u^2_{\rm rms}$.

equations in the LES region. We believe this is an incorrect argument. As we have mentioned earlier, the object of the forcing fluctuations is to *trigger* the equations to resolve turbulence, i.e. to create resolved turbulence. The fluctuations that are the most efficient for achieving this are the large-scale fluctuations. This is clearly seen from the streamwise two-point correlations of the added fluctuations (Fig. 12), the velocity profiles (Fig. 9a) and the resolved shear stresses (Figs. 10a and 13): a large streamwise correlation length (isotropic forcing, $M_S = 0.25$) gives larger resolved shear stress, and thus smaller centerline velocity, than a small streamwise correlation length (isotropic forcing, $M_S = 1$). Note that compared to the grid size, the streamwise scales of the added fluctuations are actually not large (the grid spacing in the streamwise direction is $\Delta x = 4\pi/32 \simeq 0.39$).

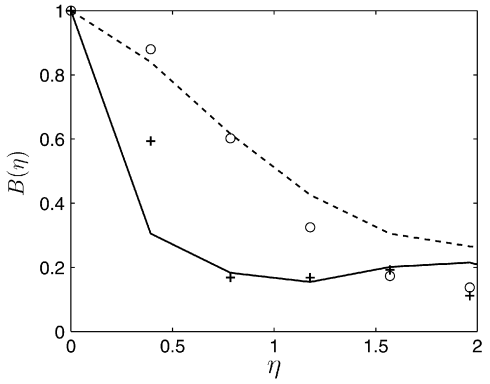

Fig. 12. Streamwise two-point correlations $B(\eta) = \langle u'(x)u'(x+\eta)\rangle/u^2_{\rm rms}$ of the added fluctuations. Solid lines: isotropic fluctuations using $M_S = 1$; dashed lines: isotropic fluctuations using $M_S = 0.25$; ○: DNS fluctuations using $M_{\rm DNS} = 0.25$; +: DNS fluctuations using $M_{\rm DNS} = 0.5$.

It can be somewhat misleading to compare shear stresses in fully developed channel flow since the total shear stress must always balance the driving pressure gradient (the first term on the right-hand side of Eq. (3)). In order to analyze the role of the shear stress in more detail, let us average the $\bar{u}$ momentum equation in the homogeneous directions (i.e. x, z and time) and integrate the resulting one-dimensional Reynolds equation from $y = 0$ to y. We then get

$$0 = \underbrace{y - \langle u'v'\rangle|_y + \left\langle (\nu + \nu_{\rm T})\frac{\partial \bar{u}}{\partial y}\right\rangle\Big|_y}_{\tau_{\rm tot}} - 1 \tag{16}$$

where the terms represent the prescribed driving pressure gradient, the resolved turbulent shear stress at y, the viscous and modelled turbulent shear stress at y, and the wall

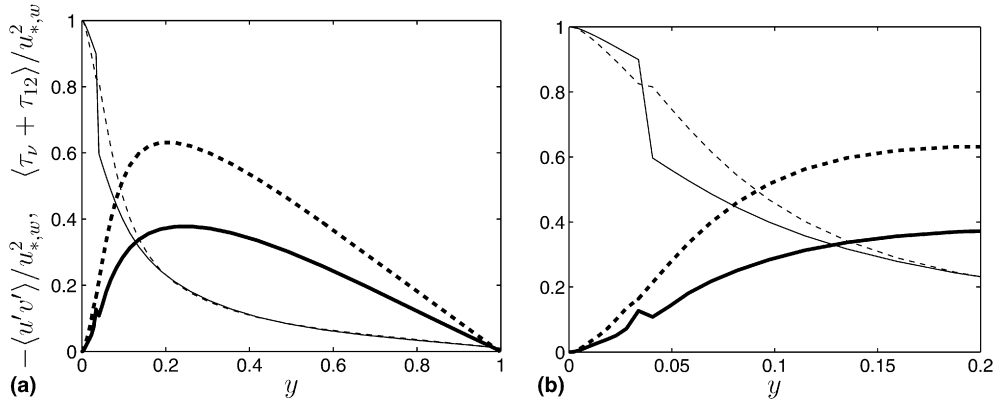

Fig. 13. Shear stresses. $M_S = 1$. τ_ν denotes viscous shear stress. Solid lines: forcing with non-isotropic fluctuations; dashed lines: forcing with isotropic fluctuations. Thick lines: resolved; thin lines: modelled. (a) Full view and (b) zoomed view.

shear stress, respectively. We obtain the usual result, that the total stress must behave as

$$\tau_{\text{tot}} = 1 - y \tag{17}$$

irrespective of the turbulence model. Note that Eqs. (16) and (17) are not valid when DNS or non-isotropic fluctuations are used, i.e. when $\langle u'_f v'_f \rangle \neq 0$, see Eq. (12). This is discussed in the next section in connection to Eq. (18).

The momentum equations adapt to satisfy a linear variation in τ_{tot} (Eq. (17)) by increasing/decreasing the time-averaged velocity gradient, whose effect is primarily to increase/decrease the modelled shear stress via an increased/decreased production of the modelled, turbulent kinetic energy, k_{T} (see Section 6.4). Fig. 10a shows that the modelled shear stress for the non-forcing case is much larger than for the forcing case. The reason is that, in order to satisfy Eq. (17), the velocity gradient is increased and thereby also ν_{T}, due to an increase in P_k and k_{T}, and the increased turbulent viscosity increases the modelled shear stress.

The relation between resolved and modelled turbulent kinetic energy, see Fig. 10b, is similar to that between the shear stresses. It can be seen that the total turbulent kinetic energy (i.e. resolved plus modelled) is strongly over-predicted both with and without forcing. This has been observed in many hybrid LES-RANS investigations (Temmerman et al., 2002; Tucker and Davidson, 2004; Davidson and Dahlström, 2005b) and is often referred to as *double counting*. The issue of overly large kinetic energies is discussed in Section 6.4.

6.3. Comparison of isotropic and non-isotropic forcing

In Fig. 14 the streamwise velocity and the turbulent kinetic energy are presented for isotropic and non-isotropic forcing conditions with $M_S = 0.25$. The velocity profile is well predicted in both cases, and the total turbulent kinetic energy is, as expected, greatly over-predicted. The resolved turbulent kinetic energy predicted with non-isotropic forcing agrees fairly well with the DNS data whereas it is over-predicted with isotropic forcing. It should be noted that this observation is entirely dependent on how the kinetic energy is scaled. Here we have chosen to scale the stresses with the wall shear stress, which is 39% larger with non-isotropic fluctuation than with isotropic fluctuations, see Table 3.

The individual, resolved RMS fluctuations are shown in Fig. 15. As can be seen, forcing affects the resolved fluctuating components differently. The largest effect is seen in the spanwise fluctuations, which are strongly increased.

The resolved shear stress, $-\langle u'v' \rangle$, is larger with isotropic forcing than with non-isotropic forcing (see Fig. 13), and this is true regardless of whether we scale with $u_{*,w}$ or u_τ. Fig. 13b shows a zoomed view of the shear stresses. For non-isotropic forcing, the large jump in the modelled shear stress at the location of the matching plane is clearly seen. The jump corresponds to the time-averaged added momentum force, $\langle S_U \rangle$ (see Eq. (10)). The global momentum balance requires that $\tau_w \equiv u^2_{*,w} = 1 + \langle S_U \rangle$, see Eq. (12), which is equal to 1.39, see Table 3. Note that in Fig. 13 the jump is equal to 0.39/1.39 since all terms in Fig. 13 are scaled with $u^2_{*,w}$. Since the time-averaged sources at the interface are not zero, i.e. $\langle S_U \rangle \neq 0$, Eqs. (16) and (17) are not valid. Eq. (17) is modified so that

$$\tau_{\text{tot}} = \begin{cases} 1 - y + \langle S_U \rangle, & y \leqslant y_{ml},\ y \geqslant 2 - y_{ml} \\ 1 - y, & y_{ml} < y < 2 - y_{ml} \end{cases} \tag{18}$$

Note that all terms in the equation above are scaled with $u^2_{*,w} > 1$.

The added momentum must be taken up by the wall shear stress in order to satisfy global momentum balance. As can be seen in Fig. 13b the modelled and viscous diffusion transport the additional momentum from the interface plane to the wall (at the interface, i.e. $y = 0.03$, the ratio between the modelled and physical viscosity is $\nu_{\text{T}}/\nu = 20$ and the ratio decreases towards the wall; at $y = 0.005$ the ratio is approximately one).

The turbulent viscosity is shown in Fig. 16. As can be seen, nothing drastic happens at the matching plane. With forcing the peak in time-averaged turbulent viscosity is

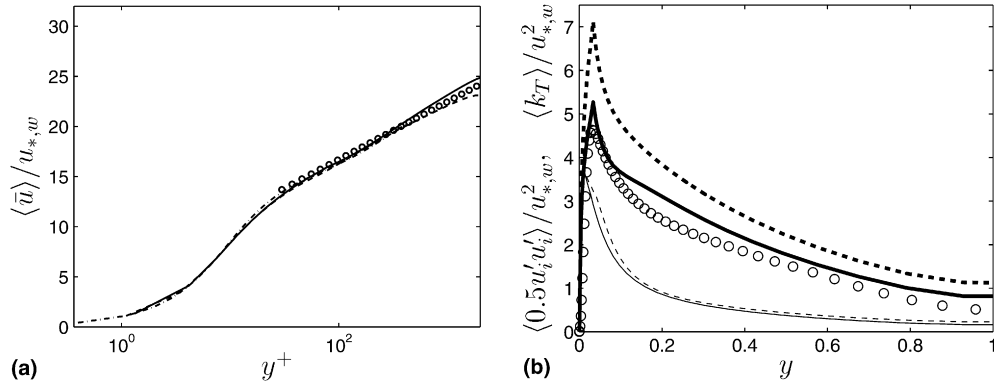

Fig. 14. Streamwise velocities and turbulent kinetic energy. $M_S = 0.25$. Solid lines: forcing with non-isotropic fluctuations; dashed lines: forcing with isotropic fluctuations. DNS data from present 96^3 DNS. (a) $\langle \bar{u} \rangle$ profiles. ○: $2.5\ln(y^+) + 5.2$; dash-dotted line: DNS. (b) Turbulent kinetic energy. Thick lines: resolved; thin lines: modelled; ○: k_{DNS}.

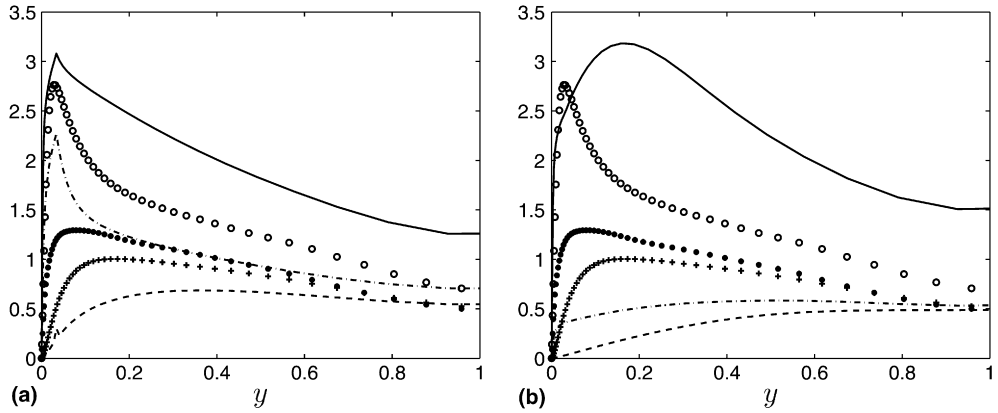

Fig. 15. Resolved RMS fluctuations. Solid lines: $u_{\rm rms}$; dashed lines: $v_{\rm rms}$; dash-dotted lines: $w_{\rm rms}$; ○: present 96^3 DNS. (a) Isotropic forcing with $M_S = 0.25$. (b) No forcing.

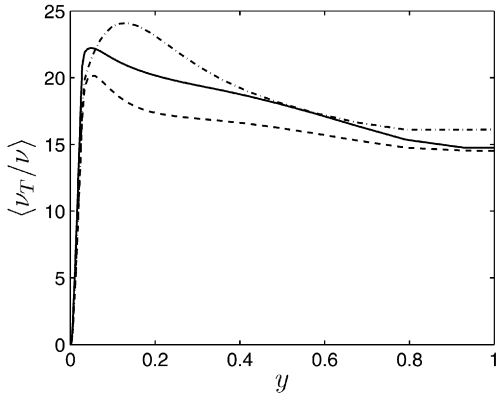

Fig. 16. Turbulent viscosity. Solid line: non-isotropic forcing; dashed line: isotropic forcing; dash-dotted line: no forcing.

located in the LES region, rather close to the matching plane ($y/\delta = 0.05$ for both isotropic and non-isotropic forcing), and with no forcing it is located further out from the wall ($y/\delta = 0.114$). It may seem somewhat surprising that the maximum turbulent viscosity is located in the LES region rather than in the URANS region, but the reason is that the grid is very coarse making the filter width, Δ, large.

The fact that the velocity profiles are well predicted (Fig. 14a) both with isotropic fluctuations ($\langle S_U \rangle = 0$) and with non-isotropic fluctuations ($\langle S_U \rangle > 0$) illustrates that it is not the time-averaged momentum source that is important; it is the dynamic properties of the momentum sources that are crucial. If a constant momentum source is added at the interface plane, the predicted velocity profile does not improve (i.e. it is the same as for no forcing); all that happens is that the wall shear stress is increased by the same magnitude. If the synthetic fluctuations are replaced by white noise, the same results are obtained as with no forcing.

One may reasonably ask why white noise does not work in the present work whereas in Piomelli et al. (2003) stochastic forcing (white noise) was used and substantial improvement was achieved (i.e. increased resolved shear stress and reduced centerline velocity). In the present work the white-noise fluctuations were generated in the same way as the DNS fluctuations in Section 5.3 (5000 instants of fluctuations along a line in the z-direction at $x = 0$). With $c_\gamma = 0.4$, see Eq. (11), no improvement was obtained compared to no forcing. c_γ was increased to 0.8 but for this value the simulations diverged due to too strong forcing. Next, the scaling with local modelled turbulent kinetic energy was omitted using $\gamma \equiv c_\gamma$. No improvement was obtained with $c_\gamma = 1$, but with $c_\gamma = 1.4$ the white-noise fluctuations manage to trigger the resolved turbulence, see Fig. 17a.

The white-noise fluctuations are generated with the same time interval as the DNS fluctuations. To obtain the fluctuations in the whole interface x–z plane, Eq. (15) is used (Taylor's hypothesis) with $M = 0.25$. It should be noted that since the forcing is white noise, both the autocorrelation and the two-point correlations are zero, i.e. $B(\tau > 0) = 0$ and $B(\zeta_i > 0) = 0$. However, since the white-noise fluctuations for $x > 0$ are taken from Taylor's hypothesis, the two-point space-time correlation

$$B(\eta, \tau) = \langle u'(x,t) u'(x+\eta, t+\tau) \rangle / u^2_{\rm rms} \tag{19}$$

is non-zero, and is equal to one where $x = V_S t$ (V_S denotes the advection speed at the interface, see Eq. (15)). In Fig. 17b it can be seen that this condition is satisfied at $(\eta/\Delta x, \tau/\Delta t) = (1,5), (2,11)$ and $(3,17)$. Further evaluation of white-noise forcing is out of the scope of the present work.

As reported in Davidson and Dahlström (2005b) the additional production introduced by the added fluctuations in the present method is large. The production of resolved turbulent kinetic energy directly related to the added fluctuation reads (cf. Eq. (9))

$$P_{k,f} = -0.5 \left\langle \gamma u'_i \frac{\partial u'_{i,f} u'_{2,f}}{\partial y} \right\rangle \tag{20}$$

which in discrete form gives $-0.5 \langle \gamma u'_i u'_{i,f} u'_{2,f} \rangle / \Delta y$, where Δy denotes the grid spacing at the interface. The additional

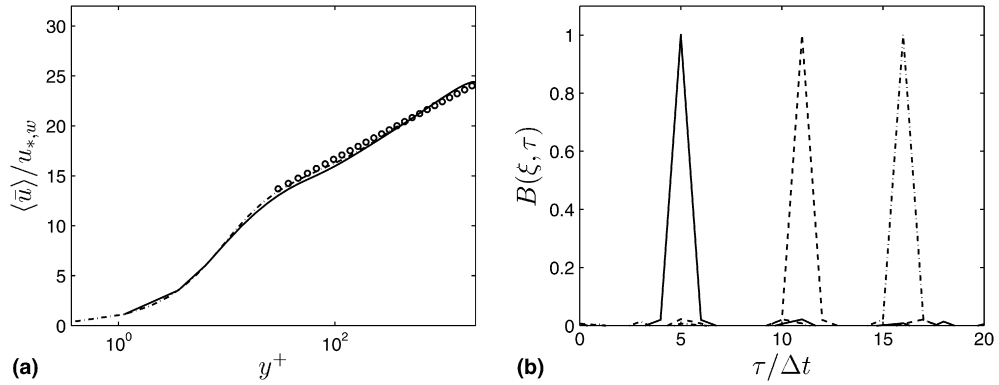

Fig. 17. Velocity profile and two-point space-time correlations. Forcing with white noise. $\gamma \equiv c_\gamma = 1.4$, see Eq. (11). (a) Velocity profile. (b) Two-point space-time correlation. Solid line: $\eta = \Delta x$; dashed line: $\eta = 2\Delta x$; dash-dotted line: $\eta = 3\Delta x$.

production, $P_{k,f}$, is actually locally more than one order of magnitude larger than the usual production, $P_k \simeq 18$, see Fig. 18 and Table 3. The predicted velocity profiles, and consequently also the resolved shear stresses, using isotropic forcing and non-isotropic forcing (Fig. 14a), DNS forcing (Fig. 9b) and white-noise forcing (Fig. 17a), all with $M_{\mathrm{DNS}} = M_S = 0.25$, are very similar. In Table 3 it can be seen that the additional production term is much larger when using white-noise forcing, indicating that white-noise forcing is inefficient compared to synthetic and DNS fluctuations in triggering resolved turbulence, which was to be expected.

The effect of different integral length scales of the forcing fluctuations is illustrated by the velocity profiles in Fig. 9. The streamwise integral length scale is enhanced by a factor of four by setting $M_S = 0.25$ and by a factor of two by reducing M_{DNS} from 0.5 to $M_{\mathrm{DNS}} = 0.25$. The two-point correlations of the forcing fluctuations are presented in Fig. 12 and the integral length scales are compiled in Table 4. (The reason why $\mathscr{L}_x$ increases only from 0.49 ($M_S = 1$) to 1.50 ($M_S = 0.25$) for the isotropic fluctuations is because of the coarse mesh, which yields inaccurate integration.) It is reasonable to artificially enhance the streamwise length scale of the forcing fluctuations considering that the streamwise resolution in the simulations is similar to the original streamwise integral length scale ($\Delta x \simeq 0.39$ and $\mathscr{L}_x \simeq 0.5$ ($M_S = 1$)). It does not make sense to add fluctuations (DNS or synthetic) whose integral length scales are similar to the grid resolution. The same argument can indeed be made for the spanwise direction, for which the situation is similar: the integral length scale is $\mathscr{L}_z \simeq 0.2$ and the resolution is $\Delta z \simeq 0.2$. No tests have been carried out with enhanced spanwise length scales.

Table 4
Integral length scales of forcing fluctuations

Forcing	M_{DNS}	M_S	$\mathscr{L}_x$	$\mathscr{L}_z$
Isotropic	–	1	0.49	0.26
Isotropic	–	0.25	1.50	0.26
Non-isotropic	–	1	0.42	0.20
Non-isotropic	–	0.25	1.61	0.20
DNS	0.5	–	0.60	0.068
DNS	0.25	–	1.06	0.08

$\mathscr{L}_x$ and $\mathscr{L}_z$ denote longitudinal and transversal integral length scales computed from the DNS or synthesized fluctuations.

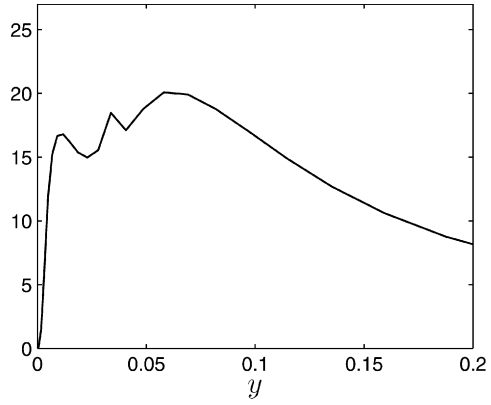

Fig. 18. Resolved production $P_k = -\langle u'v' \rangle \partial \langle \bar{u} \rangle / \partial y$. Isotropic forcing with $M_S = 0.25$.

Note that $\mathscr{L}_x$ and $\mathscr{L}_z$ are both evaluated using u' and do thus correspond to longitudinal and transversal integral lengthscale, respectively (they are denoted by Λ_f and Λ_g, respectively, in Hinze (1975)). For isotropic fluctuations the relation is $\mathscr{L}_x = 2\mathscr{L}_z$. As can be seen from Table 4, this is fairly well satisfied. It can be noted that for the non-isotropic fluctuations the ratio between the streamwise and spanwise integral length scale is even larger. This is expected since the length scales of the synthesized non-isotropic fluctuations are re-scaled (see Section 2.2).

6.4. Overly large turbulent kinetic energy

Hybrid LES-RANS predicts too high a total (resolved plus modeled) turbulent kinetic energy, which often is referred to as *double counting*, implying that the turbulence is accounted for twice (i.e by modeled *and* resolved turbulence). Indeed, it can be seen in Figs. 10b and 14b that the total turbulent kinetic energy is over-predicted. Fig. 19b presents the ratio of resolved shear stress and resolved

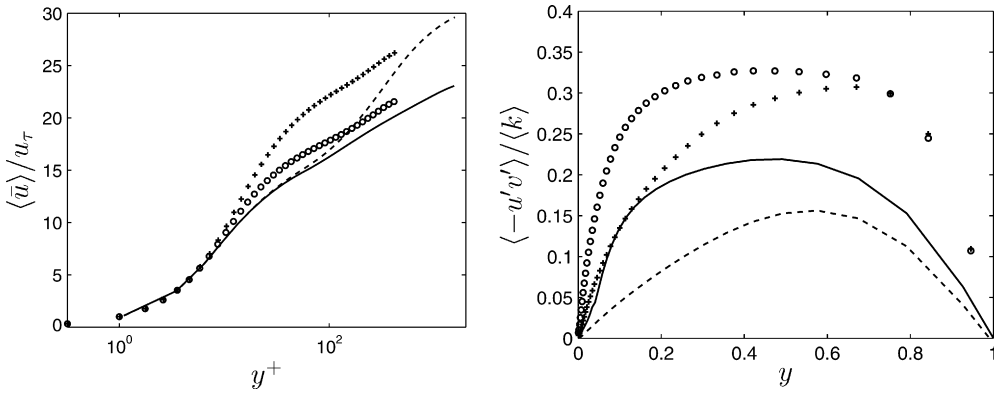

Fig. 19. Velocity profiles and ratio of resolved shear stress and turbulent kinetic energy. Hybrid LES-RANS at $Re_\tau = 2000$ and DNS at $Re_\tau = 500$. Solid line: isotropic forcing, $M_S = 0.25$; dashed line: no forcing; ○: present 96^3 DNS with $\Delta z^+ = 12$; +: present 96^3 DNS with $\Delta z^+ = 49$.

turbulent kinetic energy. The DNS data with appropriate spanwise grid spacing ($\Delta z^+ = 12$) exhibit the correct value of approximately 0.3. Hybrid LES-RANS exhibits much too small $\langle -u'v' \rangle / \langle k \rangle$ as well as too large centerline velocity (see Fig. 19a), however, as does the DNS with coarse spanwise grid spacing ($\Delta z^+ = 49$). The reason is that the mesh is too coarse to allow the hybrid LES-RANS and the coarse DNS to correctly predict the near-wall turbulence, and hence the correlation between the streamwise and wall-normal fluctuations (i.e. the shear stress) becomes too weak. Thus the equations must generate too large resolved turbulent kinetic energy to achieve the correct shear stress profile required by Eq. (17). In hybrid LES-RANS we cannot avoid this problem. We do want to use coarse grids. Unfortunately, they do not allow proper resolution of resolved turbulence. The result is too weak correlation between u' and v' and hence too large k.

In fully developed channel flow, neither the modeled nor the resolved turbulent kinetic energy enters the time-averaged momentum equations. The time-averaged momentum equations only feel the resolved shear stress and the turbulent viscosity, and this is why the overly large total kinetic energy does not give any adverse effect on the mean flow. In separated flows where all resolved stresses actively enter the time-averaged momentum equations, too large a predicted turbulent kinetic energy may have a negative impact on the quality of the predictions. In flows where the total shear stress is not dictated by the boundary conditions (i.e. Eq. (17)), an alternative scenario is that the total shear stress would be under-predicted and that the total turbulent kinetic energy equations would be well predicted.

It is, as always, instructive to look at the flow of turbulent kinetic energy, see Fig. 20. In the equation for resolved kinetic energy, $\langle k \rangle$, the modelled turbulent kinetic energy, k_T, enters the modelled dissipation term, which extracts energy from $\langle k \rangle$. This takes place through the term $\varepsilon_T \simeq 2\langle \nu_T s'_{ij} s'_{ij} \rangle$. This offers an alternative way of explaining the high level of k_T, namely that large values of k_T are necessary to make the modelled dissipation, ε_T, sufficiently large to reduce $\langle k \rangle$ to proper levels.

The production term in the k_T equation in RANS is the usual $2\nu_T S_{ij} S_{ij}$. Another fact which contributes to give large k_T is that LES and URANS have a second production term $2\langle \nu_T s'_{ij} s'_{ij} \rangle$, which produces k_T by means of the resolved fluc-

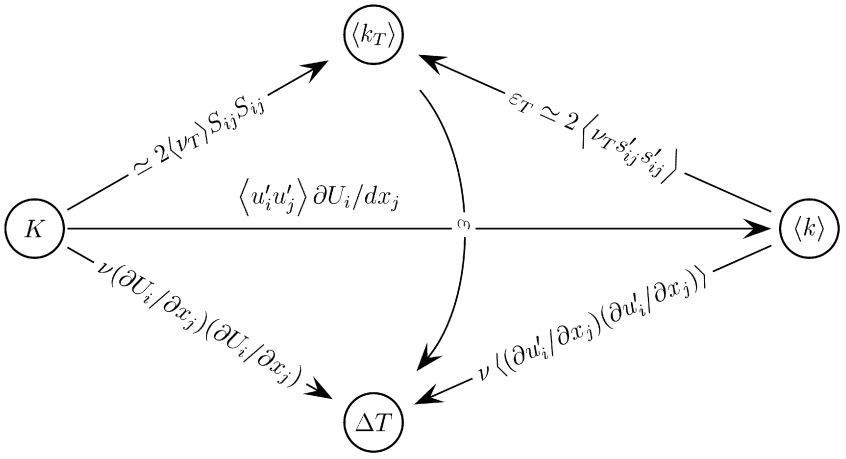

Fig. 20. Transfer of kinetic turbulent energy. The time-averaged velocity is denoted by $U = \langle \bar{u} \rangle$. $K = \frac{1}{2} U_i U_i$ and $\langle k \rangle = \frac{1}{2} \langle u'_i u'_i \rangle$ denote time-averaged kinetic and resolved turbulent kinetic energy, respectively. ΔT denotes increase in internal energy, i.e. dissipation.

tuations. This indicates that eddy-viscosity models developed and calibrated for steady RANS should perhaps be re-calibrated when used in URANS, where a significant part of the turbulence is resolved.

Fig. 20 is also useful in illustrating the main difference between LES and URANS. In (well-resolved) LES the main role of the turbulent viscosity, $\nu_T = \nu_{sgs}$, is to dissipate resolved fluctuations. The contribution of ν_{sgs} to the turbulent diffusion of momentum is negligible. In URANS, however, the role of the turbulent viscosity, $\nu_T = \nu_t$, is twofold: to dissipate resolved turbulent fluctuations and to give a non-negligible contribution to the turbulent diffusion of momentum. In the first role, ν_t is in opposition to the resolved fluctuations (the larger the ν_t, the more it will reduce the resolved fluctuations) whereas, in its second role, it cooperates with the resolved fluctuations in transporting momentum.

7. Conclusions

Hybrid LES-RANS predictions of channel flow have been presented. It is argued that the main reason why standard LES-RANS performs rather poorly is that the LES region at the interface is supplied with poor incorrect turbulent structures from the URANS region. As a result the resolved turbulent shear stress in the LES region becomes too small. To improve the performance of the model, turbulent fluctuations are added at the interface. They are added as fluctuating momentum sources. The object of the added fluctuations is to trigger to equations to resolve turbulence. The turbulent fluctuations are generated by assuming that they obey a modified von Kármán spectrum. The results obtained are considerably improved. In agreement with the findings of Piomelli et al. (2003), forcing increases the resolved shear stress, thereby reducing the centerline and bulk velocity. It is found that good results are obtained by increasing the streamwise turbulent length scale of the added turbulent fluctuations by a factor of four. The increased turbulent length scale could have been achieved by filtering out the small-scale turbulence of the forcing fluctuations before adding them to the momentum equations. When using synthesized fluctuations, this could conveniently be achieved simply by truncating the spectrum, i.e. making κ_{max} smaller, see Section 2.1. However, this approach would increase the turbulent length scale in both streamwise and spanwise direction, whereas in the present approach only the streamwise length scale was increased. It should be mentioned that in Davidson and Billson (2004) a similar approach was used. Instead of truncating the spectrum, the spectrum was extended towards smaller wavenumbers by decreasing κ_e (i.e. by increasing the turbulent length scale, L_t, used as input). The results were improved, but not as much as when increasing only the streamwise lengthscale as in the present study.

It is also found that white-noise fluctuations can be used as forcing if streamwise space-time correlations are introduced via Taylor's hypothesis. However, white-noise fluctuations are found to be less efficient in triggering the equations than DNS or synthetic fluctuations.

Forcing using four different types of fluctuations has been used in the present study: DNS fluctuations, isotropic and non-isotropic synthetic fluctuations, and white noise. The conclusion is that isotropic fluctuations offer the best solution. They require less input parameters than non-isotropic fluctuations, they do not add any momentum in the streamwise direction, and they were found to give at least as accurate results as non-isotropic fluctuations. In the present work the input used (L_t and u_{rms}) when generating the isotropic fluctuations were taken from DNS. In general, this input data can be estimated from characteristic turbulent velocity and length scales for a given turbulent boundary layer.

The present work has shown the advantage of adding forcing fluctuations. The disadvantage is that the present method is difficult to generalize in many industrial flows. On the other hand, forcing is probably not needed for separation regions but only for attached boundary layers. Still, a more general way to introduce the forcing is needed. Perhaps fluctuating momentum sources can be added in the entire URANS region as in Batten et al. (2004), Piomelli et al. (2003). As mentioned above, isotropic fluctuations are then probably a better choice that white noise. Another problem in hybrid LES-RANS is how to define the location of the matching plane. In Davidson and Dahlström (2005a,b) the flow in a plane asymmetric diffuser and the around a three-dimensional symmetric hill were simulated, and in those simulations the location of the matching plane was defined by the instantaneous streamline.

Acknowledgments

This work was financed by

the FLOMANIA project (Flow Physics Modelling – An Integrated Approach) which is a collaboration between Alenia, AEA, Bombardier, Dassault, EADS-CASA, EADS-Military Aircraft, EDF, NUMECA, DLR, FOI, IMFT, ONERA, Chalmers University, Imperial College, TU Berlin, UMIST and St. Petersburg State University. The project is funded by the European Union and administrated by the CEC, Research Directorate-General, Growth Programme, under Contract No. G4RD-CT2001-00613, and,

the DESider project (Detached Eddy Simulation for Industrial Aerodynamics) which is a collaboration between Alenia, ANSYS-AEA, Chalmers University, CNRS-Lille, Dassault, DLR, EADS Military Aircraft, EUROCOPTER Germany, EDF, FOI-FFA, IMFT, Imperial College London, NLR, NTS, NUMECA, ONERA, TU Berlin, and UMIST. The project is funded by the European Community represented by the CEC, Research Directorate-General, in the 6th Framework Programme, under Contract No. AST3-CT-2003-502842.

References

Bailly, C., Juvé, D., 1999. A stochastic approach to compute subsonic noise using linearized Euler's equations. AIAA Journal, 99–1872.

Batten, P., Goldberg, U., Chakravarthy, S., 2004. Interfacing statistical turbulence closures with large-eddy simulation. AIAA Journal 42 (3), 485–492.

Bechara, W., Bailly, C., Lafon, P., 1994. Stochastic approach to noise modeling for free turbulent flows. AIAA Journal 32 (3), 455–463.

Billson, M., 2004. Computational techniques for turbulence generated noise. Ph.D. thesis, Dept. of Thermo and Fluid Dynamics, Chalmers University of Technology, Goteborg, Sweden.

Billson, M., Eriksson, L.-E., Davidson, L., 2003. Jet noise prediction using stochastic turbulence modeling. In: 9th AIAA/CEAS Aeroacoustics Conference, AIAA paper 2003-3282.

Billson, M., Eriksson, L.-E., Davidson, L., 2004. Modeling of synthetic anisotropic turbulence and its sound emission. In: The 10th AIAA/CEAS Aeroacoustics Conference, Manchester, United Kingdom, AIAA 2004-2857, 2004.

Chorin, A., 1968. Numerical solution of the Navier–Stokes equations. Math. Comput. 22, 745–762.

Davidson, L., Billson, M., 2004. Hybrid LES/RANS using synthesized turbulence for forcing at the interface. In: Neittaanmäki, P., Rossi, T., Korotov, S., Oñate, E., Périaux, J., Knörzer, D. (Eds.), ECCOMAS 2004, Finland, July 24–28.

Davidson, L., Dahlström, S., 2005a. Hybrid LES-RANS: computation of the flow around a three-dimensional hill. In: Rodi, W., Mulas, M. (Eds.), Engineering Turbulence Modelling and Measurements, vol. 6. Elsevier, pp. 319–328.

Davidson, L., Dahlström, S., 2005b. Hybrid LES-RANS: an approach to make LES applicable at high Reynolds number. International Journal of Computational Fluid Dynamics 19 (6), 415–427.

Davidson, L., Peng, S.-H., 2003. Hybrid LES-RANS: a one-equation SGS model combined with a k–ω model for predicting recirculating flows. International Journal for Numerical Methods in Fluids 43, 1003–1018.

Davidson, L., Cokljat, D., Fröhlich, J., Leschziner, M., Mellen, C., Rodi, W. (Eds.), 2003. LESFOIL: Large Eddy Simulation of Flow Around a High Lift Airfoil. Notes on Numerical Fluid Mechanics, vol. 83. Springer-Verlag.

Dejoan, A., Schiestel, R., 2001. Large-eddy simulation of non-equilibrium pulsed turbulent flow using transport equations subgrid model. In: Lind-borg, E., Johansson, A., Eaton, J., Humphrey, J., Kasagi, N., Leschziner, M., Sommerfeld, M. (Eds.), The Second International Symposium on Turbulence and Shear Flow Phenomena, vol. 2, Stockholm, pp. 341–346.

Emvin, P., 1997. The full multigrid method applied to turbulent flow in ventilated enclosures using structured and unstructured grids. Ph.D. thesis, Dept. of Thermo and Fluid Dynamics, Chalmers University of Technology, Goteborg.

Hamba, F., 2003. An approach to hybrid RANS/LES calculation of channel flow. In: Rodi, W., Fueyo, N. (Eds.), Engineering Turbulence Modelling and Experiments, vol. 5. Elsevier, pp. 297–305.

Hinze, J., 1975. Turbulence, second ed. McGraw-Hill, New York.

Karweit, M., Blanc-Benon, P., Juvé, D., Comte-Bellot, G., 1991. Simulation of the propagation of an acoustic wave through a turbulent velocity field: a study of phase variance. J. Acoust. Soc. Am. 89 (1), 52–62.

Kenjereš, S., Hanjalić, K., 2005. LES, T-RANS and hybrid simulations of thermal convection at high RA numbers. In: Rodi, W., Mulas, M. (Eds.), Engineering Turbulence Modelling and Measurements, vol. 6. Elsevier, pp. 369–378.

Kraichnan, R., 1970. Diffusion by a random velocity field. Physics of Fluids 13, 22–31.

Krajnovic, S., Davidson, L., 2005. Flow around a simplified car. Part II: Understanding the flow. Journal of Fluids Engineering 127 (5), 919–928.

Larsson, J., Lien, F., Yee., E., 2005. Large eddy simulation of high Reynolds number channel flow on coarse grids. In: 13th Annual Conference of the Computational Fluid Dynamics Society of Canada, pp. 61–68.

Lee, S., Lele, S., Moin, P., 1992. Simulation of spatially evolving turbulence and the application of Taylor's hypothesis in compressible flow. Physics of Fluids A 4, 1521–1530.

Mellen, C., Frohlich, J., Rodi, W., 2003. Lessons from LESFOIL project on large eddy simulation of flow around an airfoil. AIAA Journal 41 (4), 573–581.

Moser, R., Kim, J., Mansour, N., 1999. Direct numerical simulation of turbulent channel flow up to $Re_\tau = 590$. Physics of Fluids A 11, 943–945.

Nikitin, N., Nicoud, F., Wasistho, B., Squires, K., Spalart, P., 2000. An approach to wall modeling in large-eddy simulations. Physics of Fluids A 12 (7), 1629–1632.

Piomelli, U., Balaras, E., Pasinato, H., Squire, K., Spalart, P., 2003. The inner–outer layer interface in large-eddy simulations with wall-layer models. International Journal of Heat and Fluid Flow 24, 538–550.

Robinson, S., 1991. Coherent motions in the turbulent boundary layer. Annual Review of Fluid Mechanics 23, 601–639.

Rodi, W., Ferziger, J., Breuer, M., Pourquié, M., 1997. Status of large-eddy simulations: results of a workshop. Journal of Fluids Engineering, 248–262.

Smirnov, A., Shi, S., Celik, I., 2001. Random flow generation technique for large eddy simulations and particle-dynamics modeling. Journal of Fluids Engineering 123 (2), 359–371.

Spalart, P., 2000. Strategies for turbulence modelling and simulations. International Journal of Heat and Fluid Flow 21, 252–263.

Spalart, P., Jou, W.-H., Strelets, M., Allmaras, S., 1997. Comments on the feasibility of LES for wings and on a hybrid RANS/LES approach. In: Liu, C., Liu, Z. (Eds.), Advances in LES/DNS, First International Conference on DNS/LES. Greyden Press, Louisiana Tech University.

Strelets, M., 2001. Detached eddy simulation of massively separated flows, Reno, NV, AIAA paper 2001-0879.

Temmerman, L., Leschziner, M., Hanjalić, K., 2002. A priori studies of near-wall RANS model within a hybrid LES/RANS scheme. In: Rodi, W., Fueyo, N. (Eds.), Engineering Turbulence Modelling and Experiments, vol. 5. Elsevier, pp. 317–326.

Temmerman, L., Hadžiadbic, M., Leschziner, M., Hanjalić, K., 2005. A hybrid two-layer URANS-LES approach for large eddy simulation at high Reynolds numbers. International Journal of Heat and Fluid Flow 26, 173–190.

Tucker, P., 2003. Differential equation based length scales to improve DES and RANS simulations. In: 16th AIAA CFD Conference, AIAA paper 2003-3968.

Tucker, P., Davidson, L., 2004. Zonal k–l based large eddy simulation. Computers & Fluids 33 (2), 267–287.

Xiao, X., Edwards, J., Hassan, H., 2003. Inflow boundary conditions for LES/RANS simulations with applications to shock wave boundary layer interactions. Reno, NV, AIAA paper 2003-0079.

Yang, K.-S., Ferziger, J., 1993. Large-eddy simulation of turbulent obstacle flow using a dynamic subgrid-scale model. AIAA Journal 31, 1406–1413.